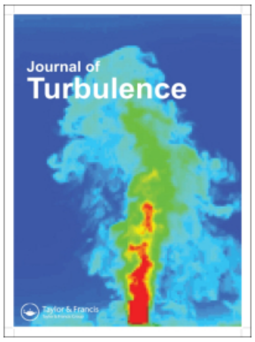

Journal of Turbulence

ISSN: (Print) (Online) Journal homepage: www.tandfonline.com/journals/tjot20

Large-scale reorientation in cubic Rayleigh–Bénard convection measured with particle tracking velocimetry

Robin Barta & Claus Wagner

To cite this article: Robin Barta & Claus Wagner (05 Dec 2024): Large-scale reorientation in cubic Rayleigh–Bénard convection measured with particle tracking velocimetry, Journal of Turbulence, DOI: 10.1080/14685248.2024.2436843

To link to this article: https://doi.org/10.1080/14685248.2024.2436843

Published online: 05 Dec 2024.

JOURNAL OF TURBULENCE
https://doi.org/10.1080/14685248.2024.2436843

Large-scale reorientation in cubic Rayleigh–Bénard convection measured with particle tracking velocimetry

Robin Barta [a,†] and Claus Wagner [a,b,†]

[a]Institute of Aerodynamics and Flow Technology, German Aerospace Center (DLR), Göttingen, Niedersachsen, Germany; [b]Institute of Thermodynamics and Fluid Mechanics, Technische Universität Ilmenau, Ilmenau, Thüringen, Germany

ABSTRACT

Three-dimensional velocity fields of a large-scale reorientation in turbulent Rayleigh–Bénard convection at $\mathrm{Ra} = 2.5 \cdot 10^9$ in a 300 mm cubic water cell are measured using particle tracking velocimetry. Reorientations are rare events occurring about once every three days in our setup, involve the large-scale circulation switching between cell diagonals. The dominant flow structures of the reorientation are extracted from the measurement data using POD supported by symmetries of the cubic cell to mimic long time series of reorientation events. The decomposition reveals degenerate mode pairs. The first six modes of the decomposition account for about 70% of the total energy and contain the major coherent structures. Modes 1-3 reflect the orientation and dynamics of the large-scale circulation, and modes 4-6 provide the orientation and dynamics of the corner circulations. A pure *Y* roll structure is observed in the middle of the reorientation event.

ARTICLE HISTORY
Received 1 August 2024
Accepted 12 November 2024

KEYWORDS
Rayleigh–Bénard convection; reorientation; coherent structures; PTV; POD

1. Introduction

Rayleigh–Bénard convection [1–5] is a canonical system for studying convective flows, where a fluid is heated from below and cooled from above in a closed cell, optimally with adiabatic side walls. The system is controlled by the Rayleigh and Prandtl number:

$$\mathrm{Ra} = \frac{g\,\lambda\,\Delta T\,L^3}{\nu\,\kappa} \quad , \quad \mathrm{Pr} = \frac{\nu}{\kappa}. \tag{1}$$

In Equation (1), g is the absolute value of the gravitational acceleration on Earth, λ is the coefficient of thermal expansion, $\Delta T = T_H - T_C$ is the temperature difference between the heating (T_H) and cooling (T_C) plates, ν is the kinematic viscosity, κ is the thermal diffusivity, and L is the cell height. For sufficiently high Ra, the density difference between the ascending warm fluid and the descending cold fluid creates typical convective flow structures depending on the shape of the cell, which is determined by the aspect ratio Γ [6,7]. In the case of cells with large aspect ratios $\Gamma > 1$, multiple superstructures emerge throughout the volume [8,9], whereas in the cell with small aspect ratios $\Gamma < 1$, a dominant quasi two-dimensional structure is found, known as the large-scale circulation (LSC), which is coupled to smaller Corner Circulations (CC) near the boundaries of the cell [10–12]. The LSC is a metastable state that persists for long periods of time and rotates clockwise or counterclockwise in the cell [13,14]. In quasi two-dimensional cells rare reversal or cessation events are of interest for many researcher, which correspond to events in which the LSC orientation disrupts and rearranges itself in a different orientation, and the mechanism behind these events is understood in recent years, see [3,10,13,15–17] among others. An special case is the aspect ratio $\Gamma = 1$, which is part of current research where experiments or simulations are performed in cubic [18–21] or cylindrical cells [22–24]. In the case of cubic cells, the LSC is extended along one of the cell diagonals [25–28] and several CC can be found in each corner of the cell. The reorientation events of the LSC in cubic cells are distinguished in two cases, the cessation reorientation and the rotation reorientation [3,29,30], which was shown first by Brown and Ahlers [3] in cylindrical cells. A cessation reorientation defines the event when the LSC stays in the same

CONTACT Robin Barta robin.barta@dlr.de
[†]These authors contributed equally to this work.

cell diagonal but changes its direction of rotation. A rotation reorientation corresponds to the event when the rotation direction stays the same, but the LSC rotates into a different cell diagonal. In an ideal system, all reorientations must occur with equal probability in a long time average based on the symmetries in the system [31]. The mechanism behind reorientation in 3D cubic cells is part of current research and several models have been developed to understand the phenomena. In Ji and Brown [32] a low dimensional model is derived to describe and predict reorientation events, in Soucasse et al. [31,33], the flow fields are decomposed using POD (proper orthogonal decomposition) and the modes are used to model the dynamics of the reorientation process, in Vishnu et al. [21] an energy transfer mechanism during reorientation events is analysed, and in Maity et al. [34] a Markov chain formalism is used to understand the reorientation transition. Most studies focusing on reorientation events rely on direct numerical simulations (DNS). The reason is that DNS provide the already fully resolved velocity and temperature field, and they are performed for an ideal setup. The latter is important since it is well-known that a small tilt of the cell against gravity can suppress the occurrence of reorientation events [3]. However, high Ra simulations are expensive and the likelihood of observing a reorientation event is reduced when the flow becomes more turbulent [15]. DNS data found in the literature are mostly in the range $\mathrm{Ra} < 10^9$. In [20] it is shown with a sensor-based temperature measurement that reorientation events at $\mathrm{Ra} \geq 10^9$ in a fully turbulent cubic Rayleigh–Bénard convection cell can be detected in long-term experiments, although they are very rare. Bai et al. [35] provided an analytic model to estimate the mean reorientation frequencies in cubic cells but most data is found for $\mathrm{Ra} \geq 10^9$ and in the case of flows with higher Ra, there are no evidence-based statistics about reorientation events in this range.

The goal of this work is to analyse coherent structures influencing the dynamics of LSC reorientations at higher Ra values than typically used in DNS directly from 3D velocity fields obtained by long-term PTV measurements in a water-filled cubic cell at $\mathrm{Ra} \approx 2.5 \cdot 10^9$. The recorded rotational reorientation event lasts about 2.2 h and the open-source proPTV framework [36,37] is used for the PTV measurements and post-processing of the data.

The paper is structured as follows. In Section 2, we present the experimental setup, and in Section 3, we first discuss the stable LSC orientations before and after the reorientation event, and then analyse the reorientation event using proper orthogonal decomposition (POD). In Section 4 we conclude the paper.

2. Experimental setup

A water-filled cubic cell has been designed to study LSC dynamics in turbulent Rayleigh–Bénard convection. Figure 1 shows a technical drawing (a) and an image of the experiment (b) and (c). The cubic cell has an internal side length of $L = 300$ mm and consists of four 8 mm thick glass sidewalls allowing the optical access to the measurement volume, glued together with silicone and glued to a black anodised aluminium plate heated from below with an electric heating mat. The heating plate of the Rayleigh–Bénard cell is mounted on a levelling table. The tilt of the cell is adjusted to less than 0.1° in each direction. A 2 mm thin layer of silicone is applied to the top edges of the glass plates to provide a watertight seal with the loose, water-cooled, black anodised aluminium cooling lid that can be placed on top of the cell. The cooling cover is held in place by four steel rods screwed into the heating plate, and nuts are applied to the steel rods to secure the cooling cover. The cooling lid has a recess that fits exactly into the square opening in the glass sidewalls.

This means that the cooled surface inside the cell is below the silicone layer and there are no inhomogeneous boundary conditions due to different materials besides of glass and aluminium. The temperature of the heating and cooling plates is measured by 8 equidistantly distributed PT100 sensors placed in both plates at a distance of 1 mm to the cell interior, and their signals are used to control the set temperature T_H and T_C of the heating and cooling plates, respectively, with a PID controller. The experiment is enclosed in a housing of insulating foam and the air temperature around the experiment is kept at the average cell temperature $\bar{T} = (T_H + T_C)/2$ by a ventilation system. The heat loss at the glass sidewalls is about 10% relative to the energy needed to create the temperature gradient in the cubic cell. With this setup turbulent flows with $3 \cdot 10^8 < \mathrm{Ra} < 1 \cdot 10^{10}$ can be realised by increasing the temperature gradient between the heating and cooling plates. Usually, a temperature gradient $\Delta T = T_H - T_C < 7$ K is used in our experiments around an average cell temperature of $\bar{T} = 20^\circ$C because it makes the air conditioning around the experiment easier. According to Gray and Giorgini [38], Weiss et al. [39] non-Oberbeck-Boussinesq effects [40] are to expect mainly for our setup with $\Delta T > 13$ K at $\bar{T} = 20^\circ$C. However, in the vicinity of the heating and cooling plates,

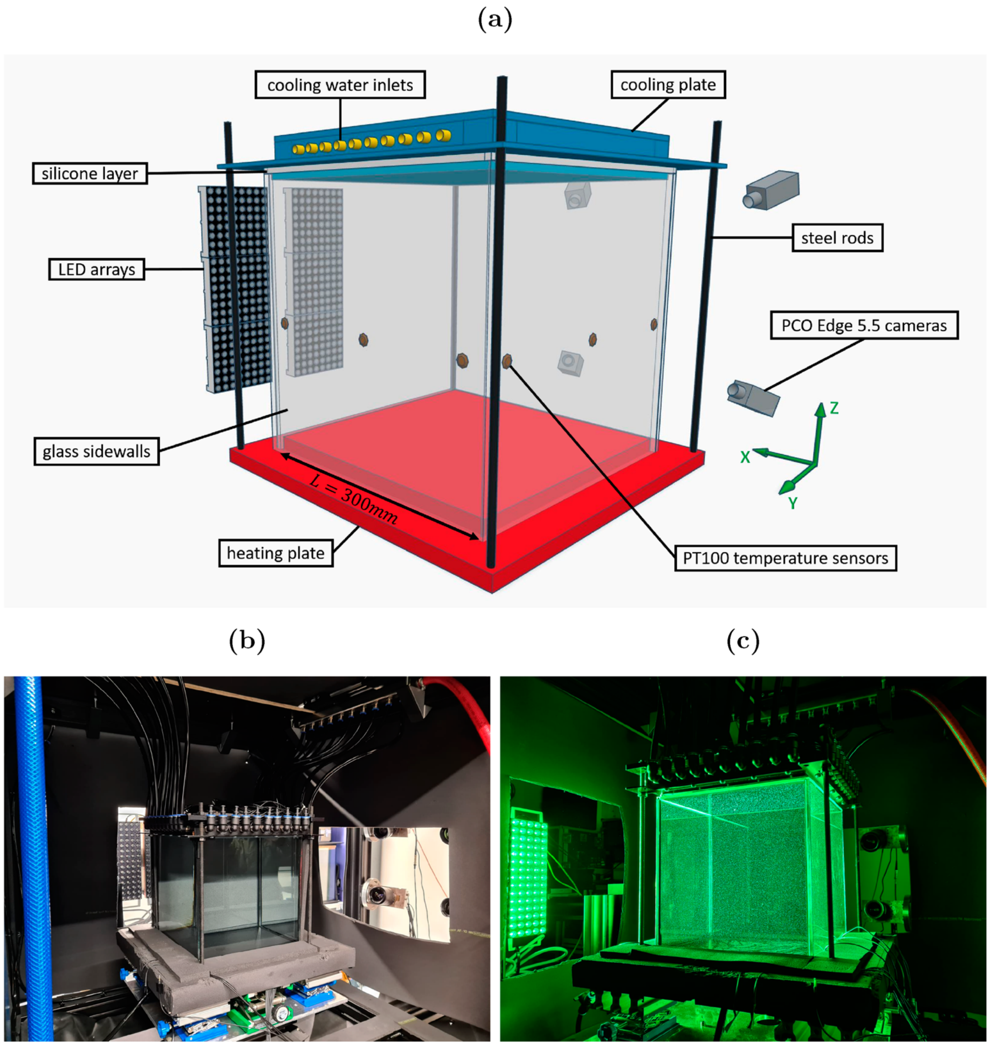

Figure 1. Experimental setup of a cubic Rayleigh–Bénard convection cell with an inner side length of 300 mm. **(a)** Technical drawing of the setup. **(b)** Photograph of the experiment. **(c)** Particle visualisation in the cell upon illumination from the side with LED arrays.

such effects can still occur locally in our measurements, but they do not significantly affect the reorientation dynamics we are interested in and are neglected.

Two high power LED arrays are used to illuminate the interior of the cells. To visualise the flow, spherical polyamide particles from LaVision are seeded into the flow. The seeding particles have an average diameter of 20 μm and are nearly buoyancy-neutral with a density of 1.03 g/cm^3 at 20 °C. The scattered LED light is captured by four PCO Edge 5.5 cameras with a pixel size of 6.5 × 6.5 μm and a resolution of 2560 × 2160 pixels. All four cameras are all installed on the same side of the cubic cell at approximately 1 m from the glass with an angle of 45°-60° to each other [41]. The LED arrays are placed on the side at 90° to the cameras as shown in Figure 1. Six PT100 temperature sensors are mounted on the outside of the side wall at mid-height to detect reorientation events of the LSC. The sensors are labelled by 1 through 6 from right to left in the top image of Figure 1.

The camera system is calibrated to the coordinate system shown in Figure 1 using a square calibration plate with 19 × 19 imprinted markers. The origin of the coordinate system is placed on the inside of the cell in the lower left corner from the camera view closest to the cameras. This is done using proPTV with its Soloff model calibration. Calibration involves removing the cooling lid and placing a socket on the top of the cell to which the calibration plate can be attached. Then, the calibration plate is moved through the cell at five positions with $Y \in \{26, 88, 150, 212, 274\}$ mm. The marker points are separated by 15 mm in each direction of the plate and each marker has a diameter of 1.5 mm.

At the beginning of a PTV measurement, the cooling lid is removed and tracer particles are seeded into the cell. After closing the cooling lid, the desired temperatures of the heating and cooling plates are set. The system is always allowed to equilibrate for approximately 11 h before image recording begins. Each measurement is limited by the fact that particles sediment on long time scales and that we can only seed particles at the beginning of the measurement without disturbing the flow. This limits the duration of each measurement to about 30 h, until an unreasonably low particle density is reached for PTV processing. Many measurements are needed to search for rare reorientation events.

3. Results

Figure 2 shows the temperature sensor signals of the averaged heating and cooling plate signal and the signals from the six sensors attached to the outer sidewalls of the cell, which are used to detect reorientation events, from one of our measurements lasting about 30 h. A temperature gradient of $\Delta T \approx 6.6$ K around $\bar{T} \approx 19.7\,°$C is used and the system parameters are approximately: Ra $\approx 2.5 \cdot 10^9$, Pr ≈ 7.

Approximately 11 h into the measurement, the LSC is stable for an extended period of time, as the temperature sensor signals in Figure 2(b) are nearly stable, and PTV image recording is started for 17 h which is indicated by the solid vertical black lines in the Figure 2 with a recording rate of 5 Hz synchronised for all cameras. This results in a total of 306000 images per camera. The seeding particles move an average of 6 pixels between two consecutive images. A reorientation event is observed in the 17 h of recording, about 2 h after the first image is taken, and the event is marked by the dashed vertical black lines in Figure 2.

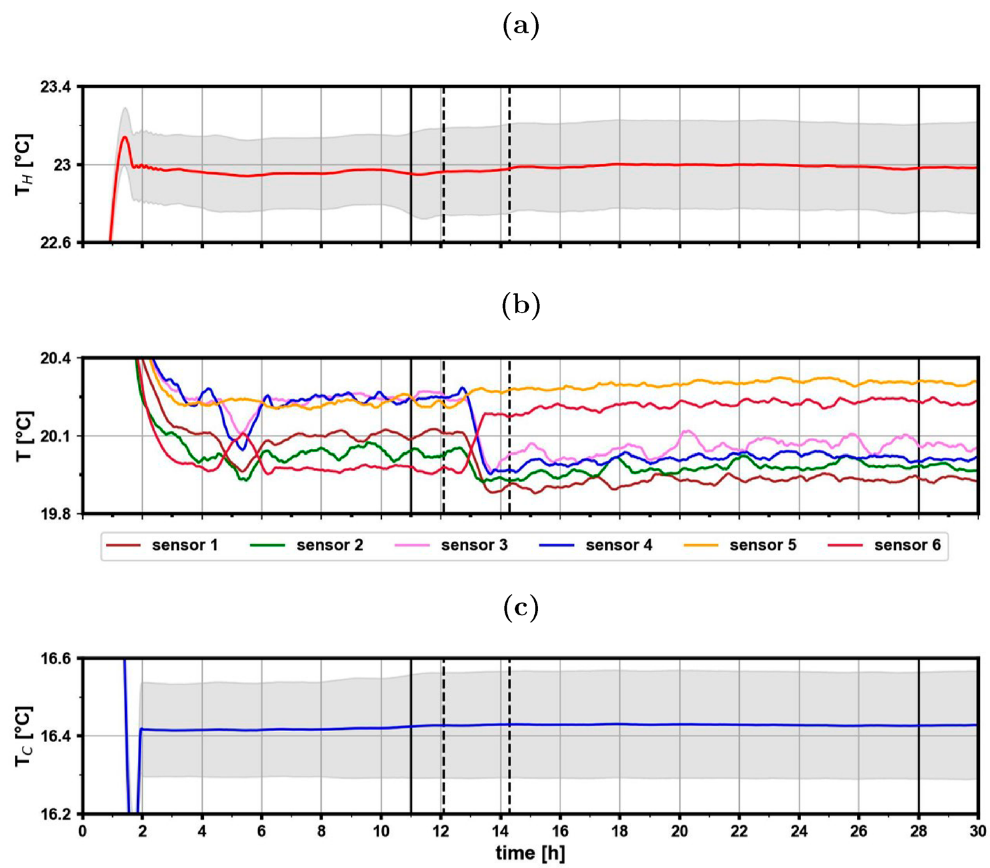

Figure 2. Temperature sensor signals during measurement. **(a)** Averaged sensor signal from eight sensors placed in the heating plate with its standard deviation. **(b)** Signals from six sensors placed on the outside of the side walls of the convection cell at the mid-height of the cell. **(c)** Averaged sensor signal from eight sensors placed in the cooling plate with its standard deviation. The solid vertical black lines indicate the time of image recording and the dashed vertical black lines indicate the detected reorientation.

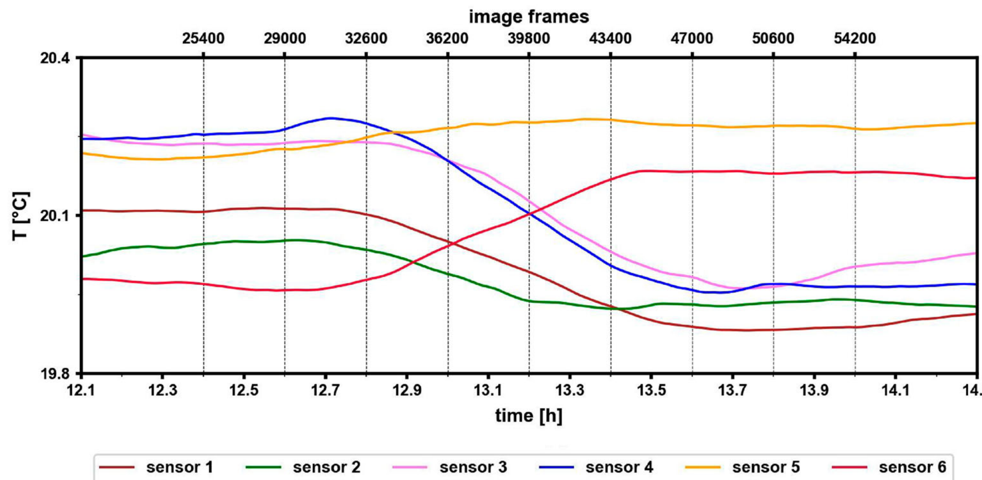

Figure 3. Temperature sensor signal from six PT100 sensors mounted on the mid-height sidewalls and specific time and image frames are indicated by vertical lines during the reorientation event.

As a result, the sidewall temperature sensor signals quickly change their value to a new stable configuration. For example, sensors 3 and 4 are located in the corner of the cubic cell where the warm uprising part of the LSC is located before the reorientation, and therefore their temperature drops drastically after the reorientation. On the other hand, the temperature of sensor 6 increases drastically during the reorientation event because the warm uprising part of the LSC turns into the corner of the cell where the sensor is located. The reorientation event covers 40000 images ($\approx$2.2 h or 144 turnover times) from the recorded time frames 20000 to 60000 and all these time steps are processed with proPTV in order to obtain particle trajectories.

The mentioned turnover time of the LSC, $\tau \approx 55$ s in our experiment, is estimated by the method used by Sakievich et al. in [42], which defines the time required for a tracer particle to travel a distance equal to two times the cell height divided by the time-averaged absolute vertical velocity maximum, about 11 mm s^{-1} in our experiment, during a stable LSC orientation.

Figure 3 shows a zoomed view of the temperature signals from the temperature sensors at mid-height cell level during the LSC reorientation.

The black vertical lines in Figure 3 indicate nine specific times and image frames during the reorientation and Figure 4 shows the reconstructed PTV trajectories for 100 time steps at these nine instances during the 2.2 h event. The number on top of each panel indicates the corresponding image frame by the vertical lines in Figure 3.

For a better visualisation, the position of the six temperature sensors at mid cell height are marked in the first panel of Figure 4. The black arrows in each panel of Figure 4 indicate the orientation of the LSC estimated by connecting the time averaged position in space with the highest positive vertical velocity and the position with the lowest negative vertical velocity. It is clearly visible that the analysed time interval around the reorientation can be divided into three phases: (i) 12.1–12.7 h, stable LSC orientation along the $Y = L{-}X$ cell diagonal. (ii) 12.7–13.7 h, LSC reorientation. (iii) 13.7–14.3 h, stable LSC orientation along the $Y = X$ cell diagonal. The Lagrangian velocity fields in Figure 4 show a rotation of the LSC from one into another cell diagonal. As the LSC changes its orientation along the cell diagonals it maintains its direction of rotation, the event is identified by a rotational reorientation. During the event a pure Y-roll structure, most dominant at frame 39800, of the LSC can be observed, which is a typical phenomenon in between a reorientation, see [31].

The number of tracer particles that are not sedimented over the course of the measurement is shown in Figure 5. The dotted red line indicates the number of particles triangulated at the corresponding time step. An exponential scaling law gives a sedimentation time as half-life time of about 23.2 h and that there were $>$ 20000 particles initially seeded in the cell. However, this value is biased by the inhomogeneous size distribution of the tracer particles, with larger particles sedimenting faster than those observed later in the experiment, and the actual value should be way bigger.

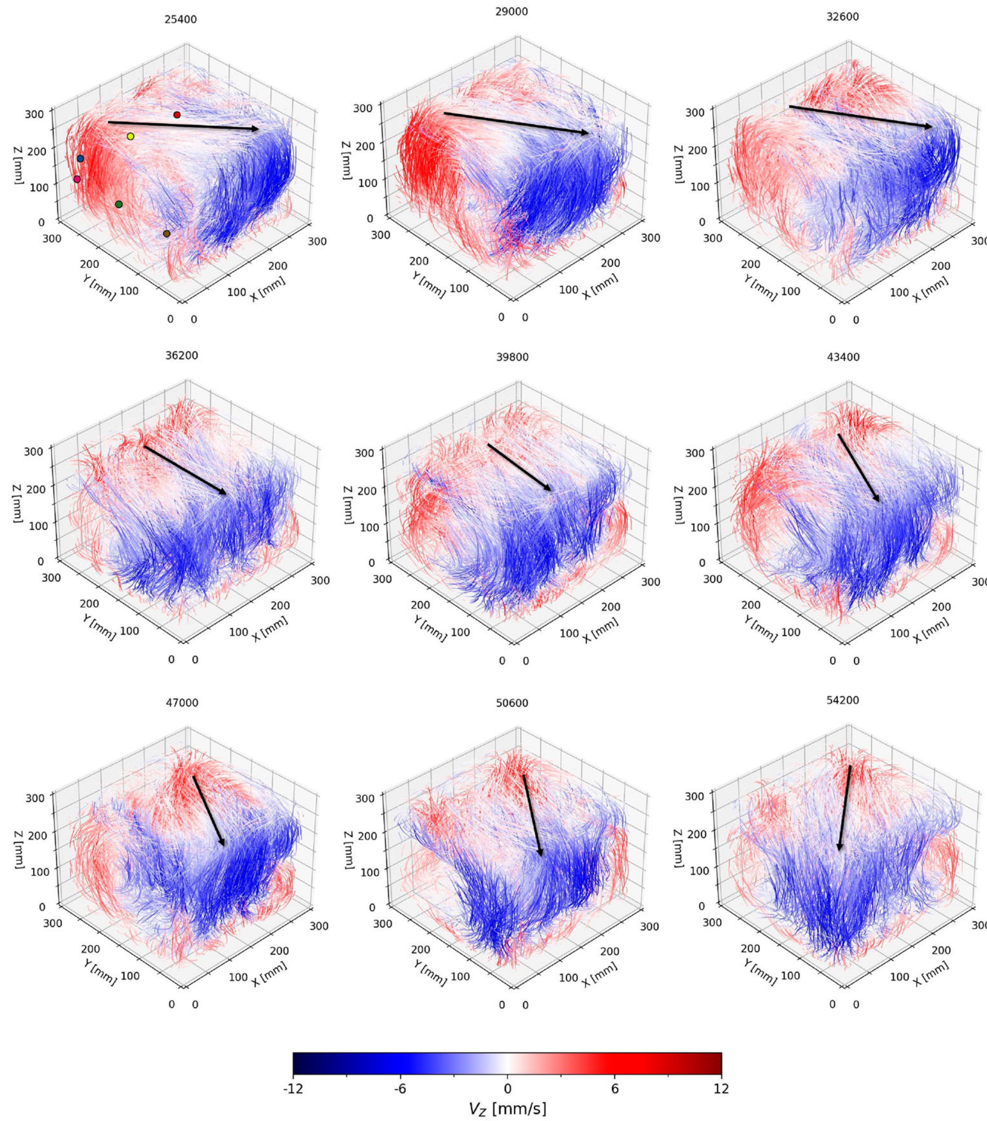

Figure 4. Tracks up to a length of 100 time steps starting from several time steps during the reorientation event indicated by the number on top of each panel, for reference, see Figure 3. The tracks are coloured by the vertical velocity component V_Z and the changing orientation of the LSC is indicated by the black arrow. The position of the temperature sensors at mid cell height are shown in first panel at image frame 25400.

In the following we analyse the LSC reorientation found in the measurement in more detail by discussing each of the observed phases (i)–(iii) individually. Most of the tools to analyse 3D velocity fields require Eulerian fields and thus we interpolate the particle tracks at each time step onto a $50 \times 50 \times 50$ equidistant grid and a divergence-free solver [36] is applied to estimate divergence-free Eulerian velocity fields.

3.1. Phases (i) and (iii) - stable LSC orientations

In phases (i) and (iii) the LSC orientation is stable along their respective diagonals. For both phases, the time-averaged vertical velocity profile at the horizontal mid-height along the respective diagonals of the LSC is calculated to provide a comparison to data found in the literature at similar system parameters. Figure 6 shows the velocity is maximum near the lateral walls and becomes small in the bulk region. The profiles at the two diagonals before and after the reorientation event are almost symmetrical and a maximum vertical velocity of about 11.2 mm s^{-1} is obtained, which corresponds to a normalised velocity of 0.2 using the free-fall velocity $V_{ff} = \sqrt{\lambda g \Delta T L} \approx 60.2$ mm s^{-1} which determines the velocity that a particle reaches under constant acceleration due to gravity. The shape of the profiles and the maximum values are in good agreement with

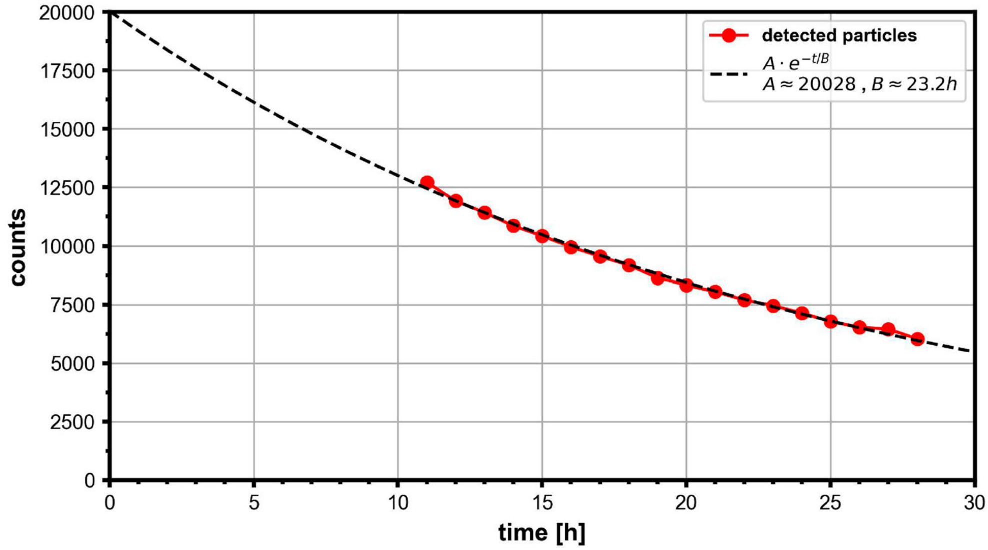

Figure 5. Sedimentation of tracer particles during the measurement. The dotted red line indicates the amount of triangulated particles at the corresponding time step. The data is fitted with an exponential decay law which is visualised as a dashed black line.

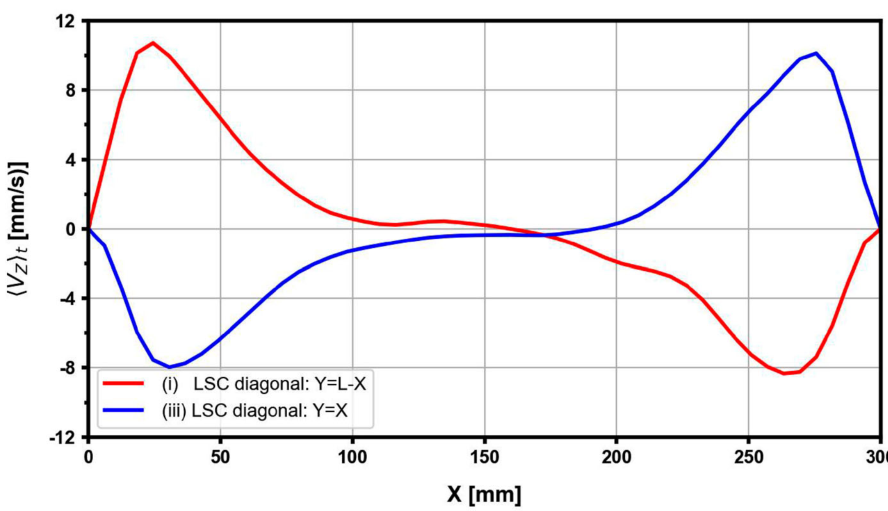

Figure 6. Time-averaged vertical velocity $\langle V_Z \rangle_t$ at the mid-height plane ($Z = 0.5L$) along the diagonal plane with $Y = L{-}X$ at state (i) containing LSC (red) and along the diagonal plane with $Y = X$ at state (iii) containing LSC (blue).

numerical studies at high Ra values [18]. However, the performed PTV does not perfectly resolve the boundary layer which is why the maxima are a little farther away from the lateral walls than it is found in DNS data [21].

3.2. Phase (ii) - LSC reorientation

Snapshots of the instantaneous Eulerian velocity fields during the observed LSC reorientation from frame 32600 to 47000 are shown in Figure 7 along both cell diagonals and along the horizontal mid-plane at $Z = 150$ mm.

The planes at $Z = 150$ mm show that the LSC rotates to a different diagonal during the reorientation, and the pure roll structure in the Y direction is visible in the middle of the event at frame 39800. Comparing the two diagonals before and after the reorientation, they look inverted, which is consistent with the observation made in Figure 6. Interestingly, there is only one corner vortex in the LSC diagonal $Y = L{-}X$ near the heating plate and near the cooling plate. The corner vortex in the LSC diagonal is either not resolved in the particle

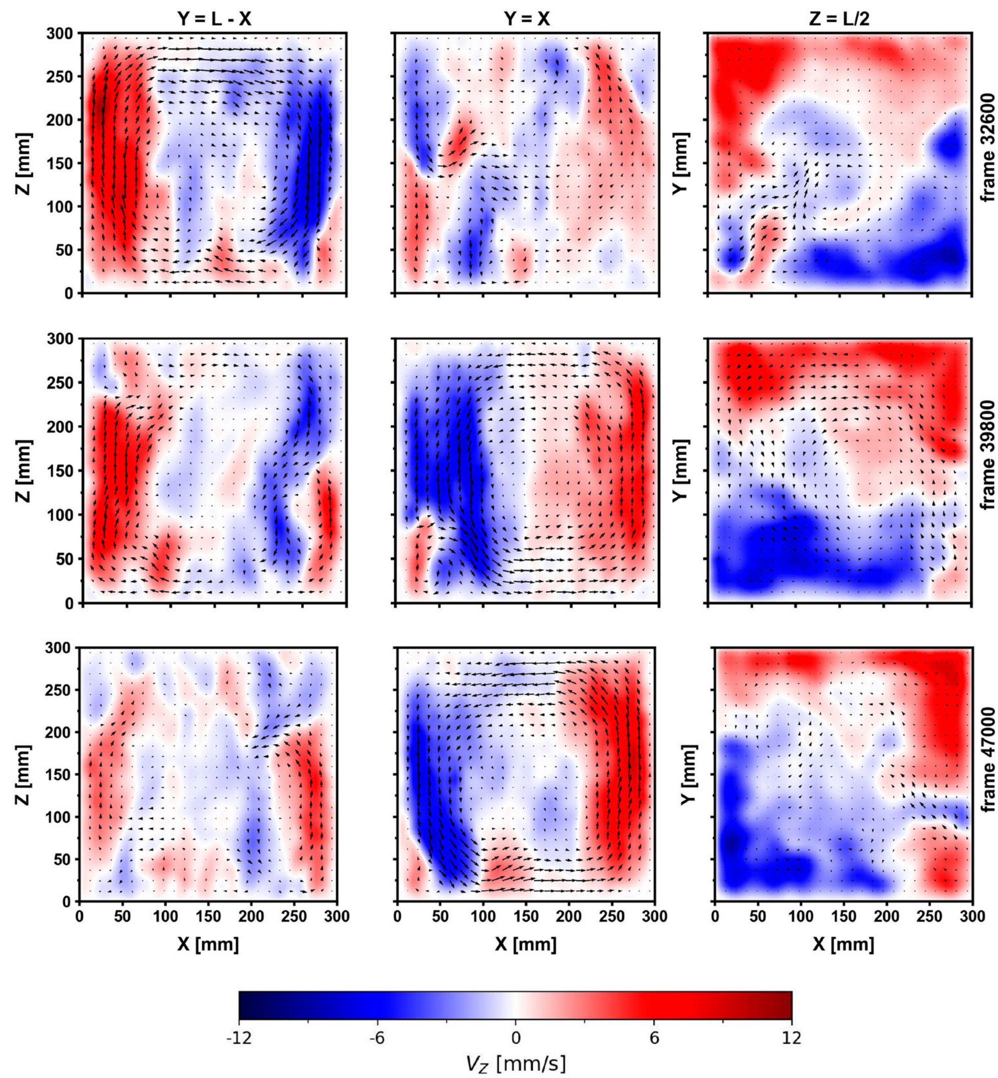

Figure 7. Velocity fields at the beginning in the **top column**, middle in the **mid column** and end in the **bottom column** of the reorientation visualised along multiple planes in the cubic cell: the diagonal plane with $Y = L - X$ in the **left row**, the diagonal plane with $Y = X$ in the **middle row** and the mid-height plane at $Z = L/2$ in the **right row** coloured by the vertical velocity component V_Z.

tracks due to its tiny size or it is not present at frame 32600 because the LSC contains much more energy and the emergence of secondary structures is suppressed [43] compared to cases studied in the literature via DNS. At a later time step, e.g. at frame 39800 a corner vortex appears near the cooling plate in the $Y = L - X$ diagonal. In the same frame, the corner vortex near the hot plate is larger and is moving toward the centre of the cell. Compared to reorientations for lower Ra and in ideal DNS data, we do not find a continuous growth of the corner vortices leading to a breakup of the LSC into corner vortices of the other diagonal, as beautifully shown by Vishnu et al. in [21]. A key observation in our experimental data is that the reorientation process takes longer than in the DNS data and is more chaotic, as the pure Y roll that is created during the reorientation fluctuates many times from one diagonal to the other, as the analysis of the proper orthogonal decomposition (POD) and the resulting modes in Figure 10 shows.

3.2.1. *Proper orthogonal decomposition using geometric symmetries*

A deeper understanding of the dynamics and the flow structures that are involved in the LSC reorientation can be gained by proper orthogonal decomposition (POD) [44–46]. The method aims at finding an optimal orthonormal basis of spatial modes $\vec{\phi}_n(\vec{r})$, time evolution coefficients $\vec{a}_n(t)$ and energy values λ_n, so that the decomposition (2) of the observed velocity field $\vec{V}(t, \vec{r}) = [V_X, V_Y, V_Z]^T$ maximises the projection of the

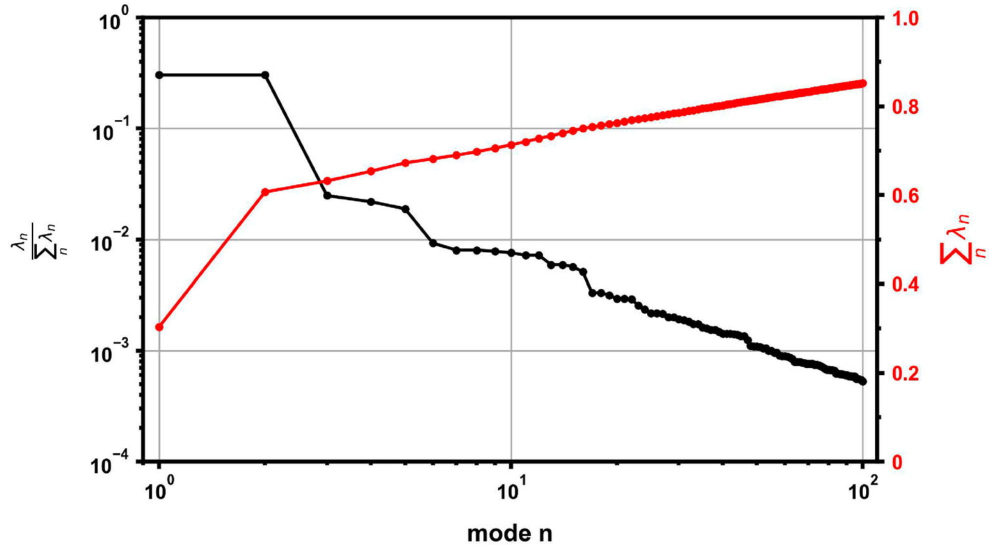

Figure 8. The POD eigenvalue spectrum of normalised eigenvalues λ_n such that $\sum_n \lambda_n = 1$ in black and the cumulated spectrum in red.

velocity field.

$$\vec{V}(t,\vec{r}) = \sum_{n=1}^{\infty} \lambda_n \vec{a}_n^T(t) \cdot \vec{\phi}_n(\vec{r}) \tag{2}$$

Our measurement data, specifically phase (ii), do not represent all LSC reorientations equally, resulting in nonequiprobable structures in the POD. This occurs because the observed event captures only one possible reorientation and in the long term, there should be no preferred orientation of the LSC, making all reorientation events equally likely. Therefore, we follow the idea of Soucasse et al. [31,33] and apply the four independent reflection symmetries (6)-(9) along the mid-planes of each coordinate direction and the cell diagonal of a cubic cell to our data. The four elementary symmetries of the problem generate a symmetry group of 16 possible symmetry combinations with which every possible configuration of the LSC and its reorientation can be mapped.

$$S_x : \begin{cases} (X,Y,Z) \rightarrow (L-X,Y,Z) \\ (V_X,V_Y,V_Z) \rightarrow (-V_X,V_Y,V_Z) \end{cases} \tag{3}$$

$$S_y : \begin{cases} (X,Y,Z) \rightarrow (X,L-Y,Z) \\ (V_X,V_Y,V_Z) \rightarrow (V_X,-V_Y,V_Z) \end{cases} \tag{4}$$

$$S_z : \begin{cases} (X,Y,Z) \rightarrow (X,Y,L-Z) \\ (V_X,V_Y,V_Z) \rightarrow (V_X,V_Y,-V_Z) \end{cases} \tag{5}$$

$$S_d : \begin{cases} (X,Y,Z) \rightarrow (Y,X,Z) \\ (V_X,V_Y,V_Z) \rightarrow (V_Y,V_X,V_Z) \end{cases} \tag{6}$$

The method of snapshots [47] is used to solve the decomposition in Equation (2). The snapshot matrix covers the three-dimensional velocity field data of the recorded reorientation event, sampled over a period of 18 frames or every 3.6 s from frame 29000 to 50600, giving a statistical set of 1201 snapshots of the velocity field. Each of the 16 elements of the symmetry group is applied to the snapshot matrix and stacked up into the final data matrix for the POD.

Figure 8 shows the energy content of each mode by visualising the normalised eigenvalues.

The cumulative energy content of the first 6 modes account for about 70% of the total energy. The decay of the energy content is slow due to the high turbulence and the three-dimensional nature of the flow. Similar

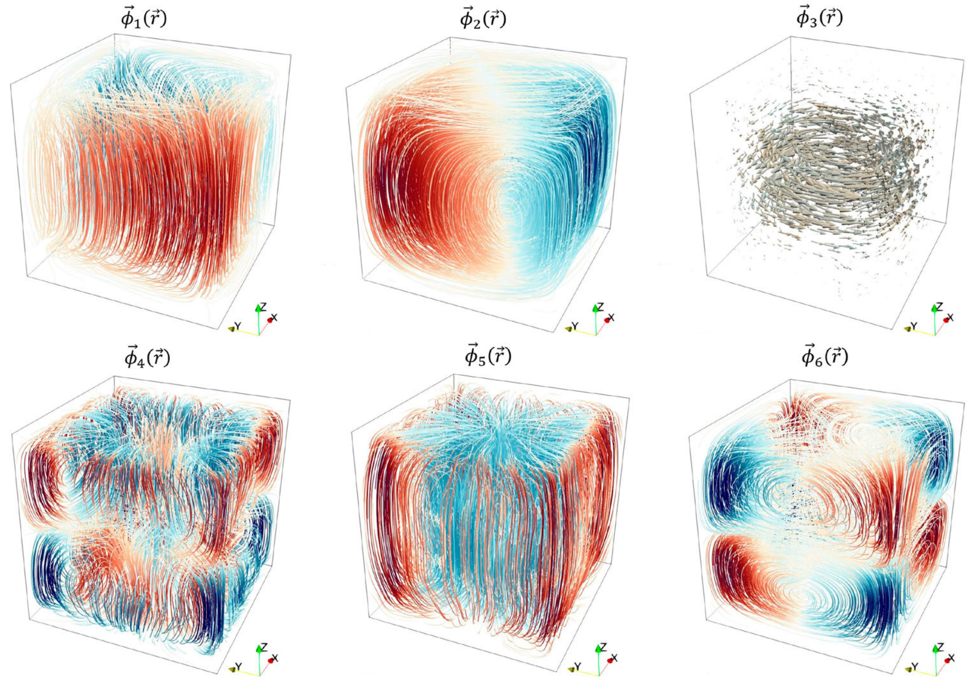

Figure 9. The first six spatial POD modes coloured by their vertical velocity component, red indicates uprising fluid and blue descending fluid.

to the POD decomposition of DNS data in [31] the first three modes make up about 60% of the total energy and the symmetry of the cubic cell, i.e. the equivalence between the X and Y axis, leads to modes which have the same energy level, e.g. mode 1 and 2 or mode 7 and 8 or 11 and 12 or 13 and 14. It is sufficient to limit the following analysis to the first six modes, since all the relevant physics of the primary and secondary structures are covered, similar to the low-order modelling by Soucasse et al. [31,33]. In contrast to [31], the temperature field is not included in the POD which helps to focus on the characteristic three-dimensional velocity structures, see Figure 9.

Modes 1 and 2, which have the same eigenvalue, represent pure diagonal roll structures. Each LSC orientation can be generated by either multiplying modes 1 and 2 by 0 or ± 1. POD modes are not uniquely defined, so multiple decomposition's can be found to generate the same flow field. This is in contrast to [31] where the prominent modes belonging to the LSC orientation are pure X and Y roll structures and by adding them a diagonal roll structure can be formed. Mode 3 is made of pure rotational flow in the horizontal plane, and thus it carries no colour in Figure 9. This mode defines the rotation direction of the LSC and in which direction the next reorientation takes place. It is the first mode with the highest energy that belongs to the reorientation dynamics which is different from what the analysis of Soucasse et al. [31] showed by including the temperature field in the POD. Mode 4 is namely the corner-circulation mode and contains eight counter-rotating structures, one in each corner of the cubic cell. The vertical velocity component in the horizontal mid-height plane is zero for this mode. Combined with one of the diagonal modes 1 or 2, mode 4 introduces the corner circulation to the flow by softening the flow in one of the two diagonal planes and increasing the flow in the other. Modes 5 and 6 are related to mode 4 and support the dynamics of the corner circulations. Mode 5 transports fluid vertically between corners in the upper half of the cube to corners in the lower half of the cube and vice versa. The vertical velocity component of mode 6 is zero near the horizontal mid-height plane, and the symmetric corner roll structures transport fluid horizontally in the upper or lower halves of the cubic cell to each other. All higher modes increase the complexity of the flow but do not add significant features such as corner circulation or other structures to it, and thus a lower-order model can be satisfied by the first 6 modes. Modes 1–3 are needed to describe the dynamics of the LSC, i.e. the primary flow structure and its reorientation. Modes 4–6 are needed to describe the dynamics of the corner circulations, i.e. the secondary flow structures.

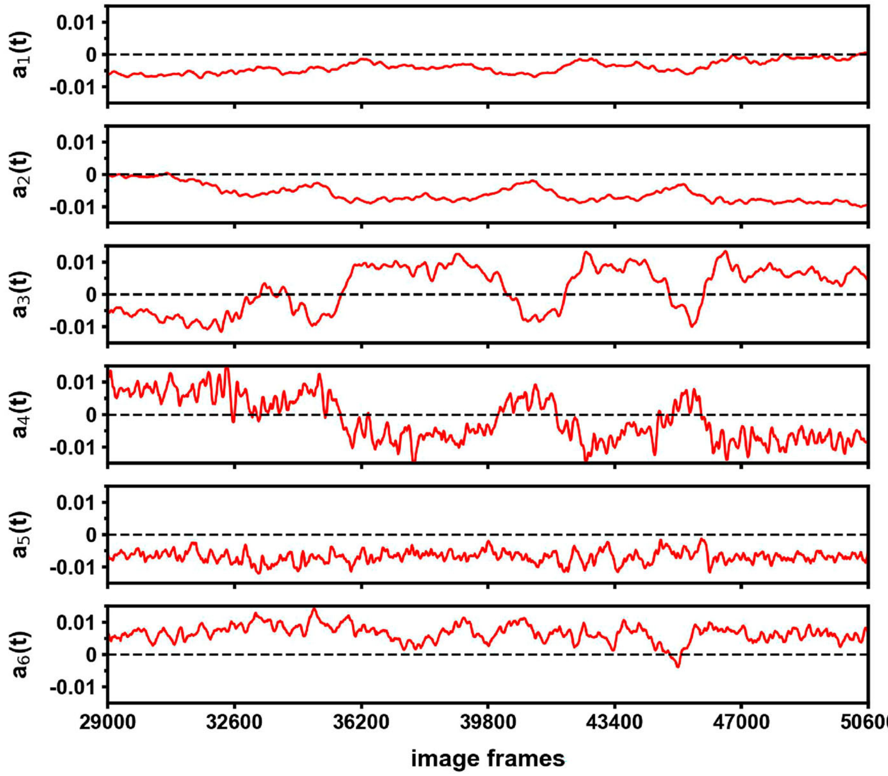

Figure 10. The first six time evolution coefficients of the POD during the PTV measurement covering the reorientation event.

The temporal dynamics of the POD modes are described by the corresponding time evolution coefficients $\vec{a}_n(t)$ shown in Figure 10.

When the LSC is stable and oriented along a cell diagonal, one of the first two modes is always close to zero. After the reorientation event, the orientation of the LSC switches to another diagonal, the previously zero value takes on a certain value, and the other time evolution coefficient becomes zero. Similar switching behaviour in the time evolution coefficients is observed in modes 3 and 4 when comparing the value at the two stable LSC orientations at frame 29000 and 50600. We see that mode 3 changes its sign several times during the reorientation event, indicating that the pure Y roll that forms during the event fluctuates between the two cell diagonals, and it takes several changes before the final flip to the other cell diagonal is stable. The dynamics of mode 3 supports the argument of Chen et al. [13] that corner circulations are not mandatory for the reorientation dynamics, but they can be Vishnu et al. [21] because it is the highest energy mode showing switching dynamics, but the mode is still related to the LSC. To find mode 3, it is important to include only velocity data in the POD, as Soucasse et al. [31] did not find such a mode by including the temperature field as well, which leads to a higher complexity in the LSC dynamics.

Figure 11 shows the reconstruction of the velocity field at frame 29000 with only the first six modes of the POD (b) and compares it with the instantaneous Eulerian velocity field (a) at this time step.

Due to the high degree of turbulence at high Ra, a slow decay of the eigenvalue spectrum is observed, and thus small scale structures can only be reconstructed by including higher modes, but the most important coherent structures such as the LSC and the corner circulations are already included in the dynamics of the first six modes. The amplitude of the reconstructed velocity field is lower because the six modes make only up to 70% of the total energy, see Figure 8. Thus the POD is able to provide an orthogonal basis which effectively denoises the experimental data and reveals the dynamics of the observed reorientation.

4. Conclusion

An LSC reorientation in turbulent Rayleigh–Bénard convection has been measured in a water-filled cubic cell with side length 300 mm at Ra $\approx 2.5 \cdot 10^9$ using PTV. In particular, Paolillo et al. [23] and Wondrak et al.

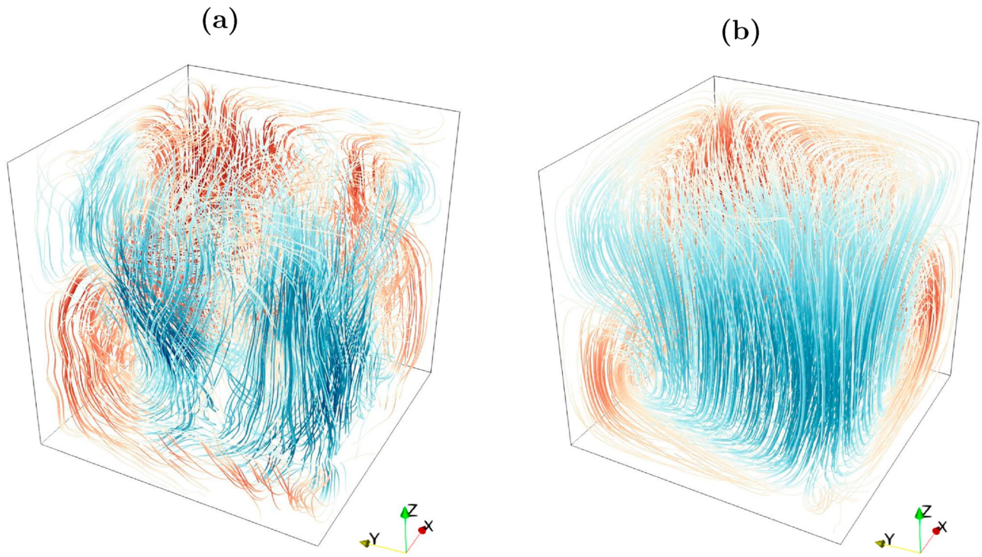

Figure 11. Reconstructed velocity field using POD modes. **(a)** Instantaneous velocity field at frame 25400. **(b)** Reconstructed (denoised) velocity field using the first six POD modes. Both fields are coloured with vertical velocity component V_Z.

[24] have experimentally studied the analysis of flow structures and characteristic modes and their dynamics in cylindrical RBC cells. Our study extends the investigation to cubic geometries and provides complementary data on LSC reorientations in this specific configuration, as comparable PTV measurements at high Ra are relatively scarce in the literature. Three-dimensional velocity fields are reconstructed using PTV over the 2.2-hour reorientation event, starting from a stable LSC orientation in one cell diagonal until the stable LSC orientation is reached in the other cell diagonal. The open-source framework proPTV is used for the PTV measurement and post-processing of the data. The rare reorientation event is found to occur about once in three days in the experimental setup. Many experimental runs were needed to observe a reorientation, because a measurement is limited to about 30 h until an unreasonable tracer particle density for PTV processing is reached, due to the long-term sedimentation of the used tracer particles and the fact that we could only seed tracer at the beginning of a measurement, since any seeding during the measurement would disturb the flow. For the nearly buoyancy-neutral seeding particles used, a half-life of about 23 h is observed. During the reorientation, a pure Y roll structure is observed, similar to events observed in DNS data from the literature [18,31]. The LSC reorientation is analysed by POD and a slow decaying eigenvalue spectrum is found due to the high degree of turbulence and the chaotic nature of the LSC reorientation [31]. Several modes have the energy level, e.g. mode 1 and 2, corresponding to diagonal roll structures, i.e. the coherent spatial structures of the LSC. The third mode first introduces the rotation of the LSC into another cell diagonal and is therefore most important in describing the reorientation dynamics. This is in contrast to the findings of Soucasse et al. [31] which included the temperature field in the POD analysis of DNS data of cubic RBC, because their low-order model is mainly based on higher order corner circulation modes. The corner circulations are relevant for the reorientation mechanism too but with lower impact as the time evolution coefficients in Figure 10 shows and their dynamics are provided by the higher modes 4, 5 and 6. Also, the POD helped to denoise the experimental data and the most important dynamics of the system are provided within the first six modes. Overall, the studied reorientation dynamics found in our experiment is in agreement with the results found in the literature generated with DNS [31], which underlines the robustness of the occurrence of LSC reorientation even in non-ideal conditions.

Acknowledgments

We thank Laurent Soucasse for sharing his detailed knowledge of POD methods for analysing LSC reorientations in cubic Rayleigh–Bénard convection cells.

Disclosure statement

No potential conflict of interest was reported by the author(s).

Data availability statement

Data might be shared upon request by email to the corresponding author.

ORCID

Robin Barta http://orcid.org/0000-0001-8882-5864
Claus Wagner http://orcid.org/0000-0003-2273-0568

References

[1] Ahlers G, Grossmann S, Lohse D. Heat transfer and large scale dynamics in turbulent Rayleigh-Bénard convection. Rev Mod Phys. 2009;81:503. doi: 10.1103/RevModPhys.81.503
[2] Bergé P, Dubois M. Rayleigh-Bénard convection. Contemp Phys. 1984;25(6):535–582. doi: 10.1080/00107518408210730
[3] Brown E, Ahlers G. Rotations and cessations of the large-scale circulation in turbulent Rayleigh-Bénard convection. J Fluid Mech. 2006;568:351–386. doi: 10.1017/S0022112006002540
[4] Grossmann S, Lohse D. Scaling in thermal convection: a unifying theory. J Fluid Mech. 2000;407:27–56. doi: 10.1017/S0022112099007545
[5] Grossmann S, Lohse D. Thermal convection for large Prandtl numbers. Phys Rev Lett. 2001;86:3316–3319. doi: 10.1103/PhysRevLett.86.3316
[6] Grossmann S, Lohse D. On geometry effects in Rayleigh–Bénard convection. J Fluid Mech. 2003;486:105–114. doi: 10.1017/S0022112003004270
[7] Shishkina O. Rayleigh-Bénard convection: the container shape matters. Phys Rev Fluids. 2021;6(9):090502. doi: 10.1103/PhysRevFluids.6.090502
[8] Moller S, Käufer T, Pandey A, et al. Combined particle image velocimetry and thermometry of turbulent superstructures in thermal convection. J Fluid Mech. 2022;945:A22. doi: 10.1017/jfm.2022.538
[9] Weiss S, Schanz D, Erdogdu AO, et al. Investigation of turbulent superstructures in Rayleigh–Bénard convection by lagrangian particle tracking of fluorescent microspheres. Exp Fluids. 2023;64(4):82. doi: 10.1007/s00348-023-03624-9
[10] Chen X, Huang S-D, Xia K-Q, et al. Emergence of substructures inside the large-scale circulation induces transition in flow reversals in turbulent thermal convection. J Fluid Mech. 2019;877:R1. doi: 10.1017/jfm.2019.624
[11] Ni R, Huang S-D, Xia K-Q. Reversals of the large-scale circulation in quasi-2D Rayleigh–Bénard convection. J Fluid Mech. 2015;778:R5. doi: 10.1017/jfm.2015.433
[12] Sugiyama K, Ni R, Stevens RJ, et al. Flow reversals in thermally driven turbulence. Phys Rev Lett. 2010;105(3):034503. doi: 10.1103/PhysRevLett.105.034503
[13] Chen X, Wang D-P, Xi H-D. Reduced flow reversals in turbulent convection in the absence of corner vortices. J Fluid Mech. 2020;891:R5. doi: 10.1017/jfm.2020.202
[14] Grossmann S, Lohse D. Fluctuations in turbulent Rayleigh-Bénard convection: the role of plumes. Phys Fluids. 2004;16:4462–4472. doi: 10.1063/1.1807751
[15] Brown E, Nikolaenko A, Ahlers G. Reorientation of the large-scale circulation in turbulent Rayleigh-Bénard convection. Phys Rev Lett. 2005;95(8):084503. doi: 10.1103/PhysRevLett.95.084503
[16] Castillo-Castellanos A, Sergent A, Rossi M. Reversal cycle in square Rayleigh–Bénard cells in turbulent regime. J Fluid Mech. 2016;808:614–640. doi: 10.1017/jfm.2016.647
[17] Zhang S, Xia Z, Zhou Q, et al. Controlling flow reversal in two-dimensional Rayleigh–Bénard convection. J Fluid Mech. 2020;891:R4. doi: 10.1017/jfm.2020.210
[18] Foroozani N, Niemela J, Armenio V, et al. Reorientations of the large-scale flow in turbulent convection in a cube. Phys Rev E. 2017;95(3):033107. doi: 10.1103/PhysRevE.95.033107
[19] Schiepel D, Bosbach J, Wagner C. Tomographic particle image velocimetry of turbulent Rayleigh-Bénard convection in a cubic sample. J Flow Vis Image Process. 2013;20:3–23. doi: 10.1615/JFlowVisImageProc.v20.i1-2
[20] Vasiliev A, Sukhanovskii A, Frick P, et al. High Rayleigh number convection in a cubic cell with adiabatic sidewalls. Int J Heat Mass Transf. 2016;102:201–212. doi: 10.1016/j.ijheatmasstransfer.2016.06.015
[21] Vishnu VT, De AK, Mishra PK. Dynamics of large-scale circulation and energy transfer mechanism in turbulent Rayleigh–Bénard convection in a cubic cell. Phys Fluids. 2020;32(9):095115. doi: 10.1063/5.0021667
[22] Bosbach J, Schanz D, Godbersen P, et al. Spatially and temporally resolved measurements of turbulent Rayleigh-Bénard convection by Lagrangian particle tracking of long-lived helium-filled soap bubbles. In: Proceedings of 14th International Symposium on Particle Image Velocimetry; Vol. 1, No. 1, 2021. p. 1–12. available at https://elib.dlr.de/143993.

[23] Paolillo G, Greco CS, Astarita T, et al. Experimental determination of the 3-D characteristic modes of turbulent Rayleigh–Bénard convection in a cylinder. J Fluid Mech. 2021;922:A35. doi: 10.1017/jfm.2021.554
[24] Wondrak T, Sieger M, Mitra R, et al. Three-dimensional flow structures in turbulent Rayleigh–Bénard convection at low Prandtl number Pr = 0.03. J Fluid Mech. 2023;974:A48. doi: 10.1017/jfm.2023.794
[25] Araujo FF, Grossmann S, Lohse D. Wind reversals in turbulent Rayleigh-Bénard convection. Phys Rev Lett. 2005;95(8):084502. doi: 10.1103/PhysRevLett.95.084502
[26] Grossmann S, Lohse D. Prandtl and Rayleigh number dependence of the Reynolds number in turbulent thermal convection. Phys Rev E. 2002;66:016305. doi: 10.1103/PhysRevE.66.016305
[27] Liu Y, Ecke RE. Heat transport scaling in turbulent Rayleigh-Bénard convection: effects of rotation and Prandtl number. Phys Rev Lett. 1997;79(12):2257. doi: 10.1103/PhysRevLett.79.2257
[28] Wei P. The persistence of large-scale circulation in Rayleigh-Bénard convection. J Fluid Mech. 2021;924:A28. doi: 10.1017/jfm.2021.619
[29] Xi H-D, Xia K-Q. Azimuthal motion, reorientation, cessation, and reversal of the large-scale circulation in turbulent thermal convection: a comparative study in aspect ratio one and one-half geometries. Phys Rev E–Stat, Nonlinear, Soft Matter Phys. 2008;78(3):036326. doi: 10.1103/PhysRevE.78.036326
[30] Xi H-D, Quan Z, Xia K-Q. Azimuthal motion of the mean wind in turbulent thermal convection. Phys Rev E. 2006;73(5):056312. doi: 10.1103/PhysRevE.73.056312
[31] Soucasse L, Podvin B, Rivière P, et al. Proper orthogonal decomposition analysis and modelling of large-scale flow reorientations in a cubic Rayleigh-Bénard cell. J Fluid Mech. 2019;881:23–50. doi: 10.1017/jfm.2019.746
[32] Ji D, Brown E. Low-dimensional model of the large-scale circulation of turbulent Rayleigh-Bénard convection in a cubic container. Phys Rev Fluids. 2020;5(6):064606. doi: 10.1103/PhysRevFluids.5.064606
[33] Soucasse L, Podvin B, Rivière P, et al. Low-order models for predicting radiative transfer effects on Rayleigh–Bénard convection in a cubic cell at different rayleigh numbers. J Fluid Mech. 2021;917:A5. doi: 10.1017/jfm.2021.260
[34] Maity P, Koltai P, Schumacher J. Large-scale flow in a cubic Rayleigh–Bénard cell: long-term turbulence statistics and Markovianity of macrostate transitions. Philos Trans R Soc A. 2022;380(2225):20210042. doi: 10.1098/rsta.2021.0042
[35] Bai K, Ji D, Brown E. Ability of a low-dimensional model to predict geometry-dependent dynamics of large-scale coherent structures in turbulence. Phys Rev E. 2016;93:023117. doi: 10.1103/PhysRevE.93.023117
[36] Barta R, Bauer C, Herzog S, et al. proPTV: a probability-based particle tracking velocimetry framework. J Comput Phys. 2023;514:113–212.
[37] Herzog S, Schiepel D, Guido I, et al. A probabilistic particle tracking framework for guided and brownian motion systems with high particle densities. SN Comput Sci. 2021;2:1–20. doi: 10.1007/s42979-021-00879-z
[38] Gray DD, Giorgini A. The validity of the Boussinesq approximation for liquids and gases. Int J Heat Mass Transf. 1976;19(5):545–551. doi: 10.1016/0017-9310(76)90168-X
[39] Weiss S, Emran M, Shishkina O. What Rayleigh numbers are achievable under Oberbeck–Boussinesq conditions?. J Fluid Mech. 2024;986:R2. doi: 10.1017/jfm.2024.389
[40] Ahlers G, Brown E, Araujo FF, et al. Non-Oberbeck–Boussinesq effects in strongly turbulent Rayleigh–Bénard convection. J Fluid Mech. 2006;569:409–445. doi: 10.1017/S0022112006002916
[41] Raffel M, Willert CE, Scarano F, et al. Techniques for 3D-PIV. In: Particle image velocimetry: a practical guide. Cham: Springer; 2018, p. 309–365.
[42] Sakievich P, Peet Y, Adrian R. Large-scale thermal motions of turbulent Rayleigh-Bénard convection in a wide aspect-ratio cylindrical domain. Int J Heat Fluid Flow. 2016;61:183–196. doi: 10.1016/j.ijheatfluidflow.2016.04.011
[43] Zhou W-F, Jun C. Similarity model for corner roll in turbulent Rayleigh-Bénard convection. Phys Fluids. 2018;30(11):111705. doi: 10.1063/1.5054647
[44] Berkooz G. Turbulence, coherent structures, dynamical systems and symmetry. Cambridge university press; 1996.
[45] Berkooz G, Holmes P, Lumley JL. The proper orthogonal decomposition in the analysis of turbulent flows. Annu Rev Fluid Mech. 1993;25(1):539–575. doi: 10.1146/fluid.1993.25.issue-1
[46] Moin P. Characteristic-eddy decomposition of turbulence in a channel. J Fluid Mech. 1989;200:471–509.
[47] Sirovich L. Turbulence and the dynamics of coherent structures. Q Appl Math. 1987;45(3):561571.